



Electronic manipulation of magnon topology by chirality injection from boundaries

Seunghun Lee, Gyungchoon Go, and Se Kwon Kim 

Department of Physics, Korea Advanced Institute of Science and Technology, Daejeon 34141, Republic of Korea

 (Received 26 September 2022; revised 3 April 2023; accepted 4 April 2023; published 20 April 2023)

Magnon bands are known to exhibit nontrivial topology in ordered magnets under suitable conditions, engendering topological phases referred to as magnonic topological insulators. Conventional methods to drive a magnonic topological phase transition are bulk magnetic or thermal operations such as changing the direction of an external magnetic field or varying the temperature of the system, which are undesired in device applications of magnon topology. In this work, we lift the limitation of the magnon topology control on the bulk nonelectronic manipulation by proposing a scheme to manipulate magnonic topological phases by electronic boundary operations of spin chirality injection. More specifically, we consider a ferromagnetic honeycomb lattice and show that a finite spin chirality injected from the boundary of the system via the spin Hall effects introduces a tunable sublattice-symmetry-breaking mass term to the bosonic counterpart of the Haldane model for the Chern insulators and thereby allows us to electronically manipulate the bulk topology of magnons from the boundary. The “shoulder” in the thermal Hall conductivity profile is proposed as an experimental probe of the chirality-induced topological phase transition. The scheme for the boundary manipulation of the magnon topology is shown to work for a honeycomb antiferromagnet as well. We envisage that the interfacial chirality injection may offer a nonintrusive electronic means to tune the static and the dynamical bulk properties of general magnetic systems.

DOI: [10.1103/PhysRevB.107.144423](https://doi.org/10.1103/PhysRevB.107.144423)

I. INTRODUCTION

Since the experimental discovery of the integer quantum Hall effect [1] and the ensuing extensive studies on topological materials [2–4], the idea of topology has been established as a powerful tool in condensed matter physics to understand exotic phases of matter and a promising resource for technical applications. Well-known electronic topological phases include a quantum spin Hall system realized in the HgTe quantum well [5] and a three-dimensional topological insulator Bi₂Te₃ [6]. These electronic topological materials are of fundamental interest as well as practical significance, for they can serve as excellent spin-current sources, enabling the efficient manipulation of spin-based devices [7–10].

While the above works are for electrons, there has been emerging attention to the topological phases of bosonic systems. In particular, the topological properties of bosonic collective excitations in ordered magnets, called magnons, have drawn physicists’ interest in that they can be easily manipulated through magnetic fields and spin torques to investigate their topological properties. In certain magnetic systems referred to as magnonic topological insulators, magnon bands are known to exhibit nontrivial topologies [11–15]. The magnonic topological insulators have been identified in various setups including honeycomb ferromagnets with magnon-magnon interaction [16,17] and magnetoelastic interaction [18].

To harness the magnon topology for practical applications, it is important to be able to manipulate the topological properties of the magnon bands. So far, the conventional control of the magnon-band topology required the bulk manipula-

tion of the systems via, e.g., changing an external magnetic field or the temperature [19]. However, these bulk magnetic or thermal operations are not only challenging to efficiently implement in nanoscale devices but also unsuitable for ultrafast execution. In this paper, we lift this limitation of the magnon-band topology control on the bulk nonelectronic manipulation by showing that the magnon-band topology can be controlled electronically from the boundary by injecting a spin chirality into the bulk. More specifically, we propose a scheme to manipulate magnonic topological phases of ferromagnets and antiferromagnets on a honeycomb lattice via chirality injection, which can be realized, e.g., via interfacial spin Hall effects resulting from the proximate heavy

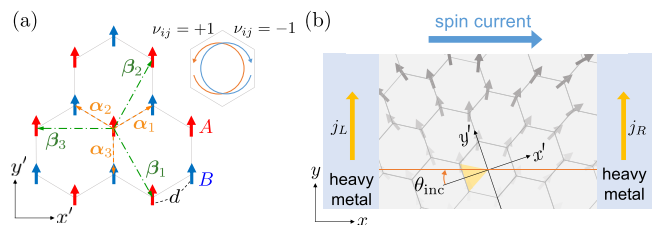


FIG. 1. (a) The ground-state spin configuration of a ferromagnetic honeycomb lattice and the sign ν_{ij} of the DM interaction. (b) The chiral spin texture is induced in a honeycomb ferromagnet by injecting a spin current into the sample with the incident angle θ_{inc} via the spin Hall effect from the proximate heavy metals. The magnon bands on top of the induced chiral texture can exhibit a topological phase transition as the injected chirality increases. See the main text for the details.

metals [20–22]. We demonstrate that the chirality injection engenders a sublattice-symmetry-breaking mass on top of the previously studied bosonic counterpart of the Haldane model [23–25]. This chirality-induced mass term competes with the known Haldane mass term, which allows us to nonlocally tune the bulk topology from nontrivial to trivial and vice versa from the boundary. For experimental probes of the chirality-induced topological phase transition, we propose the magnon thermal Hall effect arising from the band topology [26]. The “shoulders” in the thermal Hall conductivity profile can herald the presence of the proposed phase boundary. Our work exemplifies the utility of the interfacial chirality injection via the spin Hall effects as an electronic noninvasive means to control magnets and magnon bands therein.

The organization of the remainder of this paper is as follows. In Sec. II, we introduce the ferromagnetic model on a honeycomb, which is sandwiched between two heavy metals, and discuss the spin texture of its ground state. Then, in Sec. III, we employ the linear spin-wave theory to study the magnon band of the model discussed in Sec. II. Next, in Sec. IV, we discuss how the presence of spin chirality enables the manipulation of topological properties of the magnon bands. The shoulder-shaped profile of the thermal Hall conductivity, which is an experimental proxy of the chirality-induced topological phase transition, is explicated in Sec. V. We conclude with a summary and discussion in Sec. VI. Finally, details in calculations, temperature dependence of the “shoulder” pattern, and the similar topological phase transition for the honeycomb antiferromagnet model are addressed in the Appendixes A and B.

II. MODEL

We consider a two-dimensional (2D) ferromagnet on a honeycomb lattice whose Hamiltonian is given by

$$H = -J \sum_{\langle i,j \rangle} \mathbf{S}_i \cdot \mathbf{S}_j + \frac{K}{2} \sum_i S_{i,z}^2 + D \sum_{\langle\langle i,j \rangle\rangle} v_{ij} \hat{\mathbf{z}} \cdot (\mathbf{S}_i \times \mathbf{S}_j) - B \sum_i S_{i,z}, \quad (1)$$

where the first and the second terms represent the Heisenberg exchange interaction ($J > 0$) between the nearest spins and the easy-plane anisotropy ($K > 0$), respectively. The 2D honeycomb ferromagnet with an in-plane magnetic order is realized in monolayer CrCl_3 [27–29]. The third term is the Dzyaloshinskii-Moriya (DM) interaction between the next-nearest-neighboring spins [30,31]. In the DM interaction, the sign $v_{ij} = \pm 1$ depends on the orientation of the two next-nearest spins as shown in Fig. 1(a). The last term in Eq. (1) represents the Zeeman coupling to the out-of-plane magnetic field B . When $|B| < KS$, the ferromagnetic ground state has a uniform spin configuration characterized by a polar angle $\theta_0 = \cos^{-1}(B/KS)$ with the spontaneously broken $U(1)$ spin-rotational symmetry about the z axis, which is crucial for a spin current to flow through the magnet [20,32–34]. We

denote the distance between the nearest neighbors by d and that between the next-nearest neighbors by $a = \sqrt{3}d$.

Now, let us consider the setup shown in Fig. 1(b) designed for the injection of spin chirality into the magnet. The honeycomb ferromagnet is sandwiched between two heavy metals with the relative angle of θ_{inc} ($|\theta_{\text{inc}}| \leq \pi/6$). The charge currents through the two heavy metals inject a spin current polarized along the z direction into the ferromagnet via the spin Hall effect [21,35], which is also referred to as spin-orbit torque [36]. The injected spin currents from the left and the right heavy metals are given by $\tau(x=0) = \sin^2 \theta \vartheta j_L$ and $\tau(x=L) = \sin^2 \theta \vartheta j_R$, respectively, where ϑ is the dampinglike spin-orbit-torque parameter for the injected spin current per unit charge-current density [37] and L is the sample length. On the other hand, the z component of the spin current within the magnet is given by $\mathbf{J}_z^s = -\mathcal{A} \sin^2 \theta \nabla \phi$ where \mathcal{A} is the exchange coefficient. For the given charge currents j_L and j_R , we can obtain a steady-state solution by matching the bulk spin current to the injected spin currents at the two boundaries. In particular, when the charge currents on both sides are the same ($j_L = j_R = j$), which is the situation we focus on in this paper, it has been shown in Refs. [20–22] that a static spin texture with spatially varying azimuthal angle $\phi(\mathbf{r}) = \phi_0 + \phi'x$ can be established in the bulk of the magnet with the azimuthal-angle gradient $\phi' \approx j\vartheta/\mathcal{A}$ (see Appendix A2). In this case, the spin current flows with the incident angle of θ_{inc} with respect to the primed coordinate system (x', y') of the honeycomb lattice shown in Fig. 1(b). Here, note that the spin chirality ϕ' of the magnet can be nonlocally tuned from the boundary of the sample by controlling the charge currents j flowing in the adjacent heavy metals. Hereafter, we shall use the spin chirality ϕ' as a tunable control parameter of the system. When there is a finite spin chirality, the easy-plane anisotropy K is effectively renormalized to $K_{\text{eff}} = K - J[3 - g(\phi'd, \theta_{\text{inc}})]$, where $g(\phi'd, \theta_{\text{inc}}) = \sum_{j=1}^3 \cos(\nabla \phi \cdot \boldsymbol{\alpha}_j)$ and $\nabla \phi = \phi'(\cos \theta_{\text{inc}}, -\sin \theta_{\text{inc}})$ so that the ferromagnetic ground state has a modified polar angle $\theta_0 = \cos^{-1}(B/K_{\text{eff}}S)$ when $|B| < K_{\text{eff}}S$ (see Appendix A3).

III. MAGNON HAMILTONIAN

Under the chirality injection, the static steady state in the bulk of the ferromagnet is given by $\mathbf{S}_i = S(\sin \theta_0 \cos \phi_i, \sin \theta_0 \sin \phi_i, \cos \theta_0)$ where the azimuthal angle varies over space as $\phi_i = \phi_0 + \phi'x_i$. To obtain a magnon band on top of the chiral spin texture, we introduce new spin variables $\tilde{\mathbf{S}}_i = R_i \mathbf{S}_i$ for each spin where

$$R_i = \begin{pmatrix} \cos \theta_0 \cos \phi_i & \cos \theta_0 \sin \phi_i & -\sin \theta_0 \\ -\sin \phi_i & \cos \phi_i & 0 \\ \sin \theta_0 \cos \phi_i & \sin \theta_0 \sin \phi_i & \cos \theta_0 \end{pmatrix} \quad (2)$$

is the three-dimensional orthonormal matrix representing a local spin transformation that rotates the original spin \mathbf{S}_i to the z axis. The Hamiltonian for the noninteracting magnons can be obtained by rearranging Eq. (1) with new spin variables $\tilde{\mathbf{S}}_i$ and performing the Holstein-Primakoff transformation truncated

to the order of \sqrt{S} [38]:

$$\begin{aligned}\tilde{S}_{i,x} &= \sqrt{\frac{S}{2}}(c_i^\dagger + c_i), & \tilde{S}_{i,y} &= i\sqrt{\frac{S}{2}}(c_i^\dagger - c_i), \\ \tilde{S}_{i,z} &= S - c_i^\dagger c_i\end{aligned}\quad (3)$$

with $c = a, b$, where a_i and b_i are the independent bosonic operators residing in the sublattice A and B , respectively. After a Fourier transformation $c_i = \sqrt{2/N} \sum_{\mathbf{k}} c_{\mathbf{k}} e^{i\mathbf{k}\cdot\mathbf{r}_i}$ [$\mathbf{k} = (k_x, k_y)$], we can rewrite the magnon Hamiltonian in the momentum

space in the Bogoliubov–de Gennes (BdG) form with the aid of the Nambu vector $\psi_{\mathbf{k}} = (a_{\mathbf{k}}, b_{\mathbf{k}}, a_{-\mathbf{k}}^\dagger, b_{-\mathbf{k}}^\dagger)^T$:

$$H = \frac{1}{2} \sum_{\mathbf{k}} \psi_{\mathbf{k}}^\dagger \mathcal{H}(\mathbf{k}) \psi_{\mathbf{k}}, \quad (4)$$

$$\mathcal{H}(\mathbf{k}) = \begin{pmatrix} h(\mathbf{k}) & \lambda(\mathbf{k}) \\ \lambda(\mathbf{k})^\dagger & h(-\mathbf{k})^T \end{pmatrix}, \quad (5)$$

$$h(\mathbf{k}) = \epsilon_0 I + \sum_{j=1}^3 \begin{pmatrix} JS \sin^2 \theta_0 \cos \varphi_{\alpha_j} + DS f_j(\mathbf{k}, \nabla \phi) & -JS e^{i\mathbf{k}\cdot\alpha_j} \left(\cos \frac{\varphi_{\alpha_j}}{2} + i \cos \theta_0 \sin \frac{\varphi_{\alpha_j}}{2} \right)^2 \\ -JS e^{-i\mathbf{k}\cdot\alpha_j} \left(\cos \frac{\varphi_{\alpha_j}}{2} - i \cos \theta_0 \sin \frac{\varphi_{\alpha_j}}{2} \right)^2 & JS \sin^2 \theta_0 \cos \varphi_{\alpha_j} - DS f_j(\mathbf{k}, \nabla \phi) \end{pmatrix}, \quad (6)$$

$$\lambda(\mathbf{k}) = \begin{pmatrix} \frac{S}{2} \sin^2 \theta_0 \left(K - 2D \sum_{j=1}^3 e^{i\mathbf{k}\cdot\beta_j} \sin \varphi_{\beta_j} \right) & -JS \sin^2 \theta_0 \sum_{j=1}^3 e^{i\mathbf{k}\cdot\alpha_j} \sin^2 \frac{\varphi_{\alpha_j}}{2} \\ -JS \sin^2 \theta_0 \sum_{j=1}^3 e^{-i\mathbf{k}\cdot\alpha_j} \sin^2 \frac{\varphi_{\alpha_j}}{2} & \frac{S}{2} \sin^2 \theta_0 \left(K + 2D \sum_{j=1}^3 e^{i\mathbf{k}\cdot\beta_j} \sin \varphi_{\beta_j} \right) \end{pmatrix}, \quad (7)$$

where $\epsilon_0 = B \cos \theta_0 - KS(1 + 3 \cos 2\theta_0)/4 + 3JS \cos^2 \theta_0$, $\varphi_{\alpha_j} = \nabla \phi \cdot \alpha_j$ and $\varphi_{\beta_j} = \nabla \phi \cdot \beta_j$ are the azimuthal angle difference along α_j and β_j , respectively, and $f_j(\mathbf{k}) = \sin \varphi_{\beta_j} [\cos(\mathbf{k} \cdot \beta_j)(1 + \cos^2 \theta_0) - 2 \sin^2 \theta_0] + 2 \cos \varphi_{\beta_j} \sin(\mathbf{k} \cdot \beta_j) \cos \theta_0$. After neglecting the off-diagonal blocks $\lambda(\mathbf{k})$ and $\lambda(\mathbf{k})^\dagger$ that modify a magnon-band structure near the points $\mathbf{K} = (4\pi/3a, 0)$ and $\mathbf{K}' = (2\pi/3a, 2\pi/\sqrt{3}a)$ only slightly (see Appendix A4), we obtain the following magnon Hamiltonian: $H = \sum_{\mathbf{k}} \Psi_{\mathbf{k}}^\dagger [h_0 I + \mathbf{h}(\mathbf{k}) \cdot \boldsymbol{\sigma}] \Psi_{\mathbf{k}}$ where $\Psi_{\mathbf{k}} = (a_{\mathbf{k}}, b_{\mathbf{k}})^T$ and $\boldsymbol{\sigma} = (\sigma_1, \sigma_2, \sigma_3)$ are the Pauli matrices. The components of the Hamiltonian H are given by

$$h_0 = \epsilon_0 + JS \sin^2 \theta_0 \sum_{j=1}^3 \cos \varphi_{\alpha_j}, \quad (8)$$

$$\mathbf{h}(\mathbf{k}) = \sum_{j=1}^3 \begin{pmatrix} -JS \operatorname{Re}[\rho_j(\mathbf{k})] \\ -JS \operatorname{Im}[\rho_j(\mathbf{k})] \\ DS f_j(\mathbf{k}) \end{pmatrix}, \quad (9)$$

where $\rho_j(\mathbf{k}) = e^{-i\mathbf{k}\cdot\alpha_j} [\cos(\varphi_{\alpha_j}/2) - i \cos \theta_0 \sin(\varphi_{\alpha_j}/2)]^2$. The corresponding energies of the upper and the lower bands are given by

$$E^\pm(\mathbf{k}) = h_0 \pm |\mathbf{h}(\mathbf{k})|. \quad (10)$$

In the absence of the DM interaction ($D = 0$), the gap between the upper and the lower band closes at the points $\mathbf{k} = \bar{\mathbf{K}}$ and $\bar{\mathbf{K}}'$ where $\rho_j(\mathbf{k}) = 0$ holds, which are the so-called Dirac points. When no spin chirality is present ($\phi' = 0$), the two Dirac points are just \mathbf{K} and \mathbf{K}' and the gap there is given by $\Delta_{\phi'=0} = 6\sqrt{3}DS \cos \theta_0$ [23,24]. The gap $\Delta_{\phi'=0}$ closes when the DM interaction vanishes.

In the presence of spin chirality $\phi' \neq 0$, the two Dirac points $\bar{\mathbf{K}}$ and $\bar{\mathbf{K}}'$ shift from their original positions and the gap sizes at the two points change. The positions of the shifted Dirac points can be obtained by solving $\rho_j(\mathbf{k}) = 0$

perturbatively with respect to ϕ' . We can then obtain the Dirac Hamiltonian for magnons by expanding the Hamiltonian (9) near $\bar{\mathbf{K}}$ and $\bar{\mathbf{K}}'$ (see Appendix A5 for a detailed expressions for the shifted Dirac points and the Dirac Hamiltonians). The size of the modified gaps at $\bar{\mathbf{K}}$ and $\bar{\mathbf{K}}'$ is given by

$$\begin{aligned}\Delta_{\bar{\mathbf{K}}/\bar{\mathbf{K}}'} &= \frac{3\sqrt{3}|D|}{16K^2} \left| \pm 8B[4K + 3J(\phi'd)^2] \right. \\ &\quad \left. - 13K^2 S(\phi'd)^3 \cos 3\theta_{\text{inc}} \right|, \end{aligned} \quad (11)$$

to linear order in B . Note that the gap $\Delta_{\bar{\mathbf{K}}/\bar{\mathbf{K}}'}$ is proportional to the DM interaction D as previously shown [23] and also proportional to $\cos(3\theta_{\text{inc}})$ as dictated by the sixfold rotational symmetry of the honeycomb lattice. More importantly, for $D \neq 0$, there is a critical magnetic field B_c where the gap at either $\bar{\mathbf{K}}$ or $\bar{\mathbf{K}}'$ closes:

$$B_{\bar{\mathbf{K}}/\bar{\mathbf{K}}',c} = \pm \frac{13KS}{32} (\phi'd)^3 \cos 3\theta_{\text{inc}}, \quad (12)$$

to cubic order in the spin chirality $\phi'd$. The critical magnetic field is determined by the spin chirality ϕ' and thus can be controlled from the boundaries. This chirality-induced magnon-gap closing is one of our main results, whose topological significance is described in Sec. IV.

IV. TOPOLOGICAL PHASE TRANSITION

The band topology of the bosonic quadratic Hamiltonian [Eq. (9)] is identical to that of the corresponding fermionic counterpart with the same Hamiltonian [39]. Note from Eq. (11) that the mass term of the Dirac Hamiltonian [Eq. (9)] contains two components. The first component is the Haldane mass [4] proportional to DB and its sign is different between the two Dirac points $\bar{\mathbf{K}}$ and $\bar{\mathbf{K}}'$. This manifestation of the Haldane model at the honeycomb ferromagnet

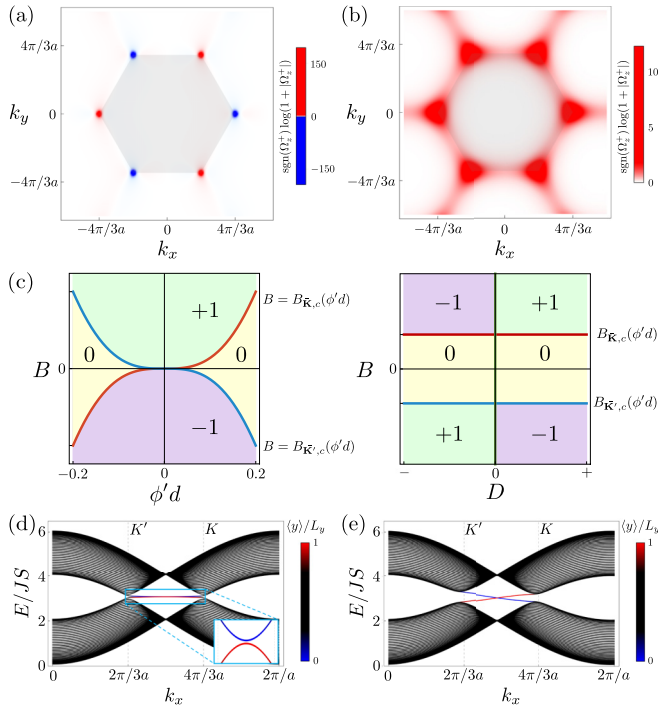


FIG. 2. (a) The Berry curvature Ω_z^+ of the upper magnon band in a honeycomb ferromagnet under chirality injection $\phi'd = 0.2$ for $B = 0$ and (b) for $B = 0.05JS$. (c) The topological phase diagram, which shows the Chern number of the upper magnon band. (Left panel: $D > 0$ is fixed, right panel: $\phi'd > 0$ is fixed.) The red and blue curves show the phase boundaries between the trivial and nontrivial phases [Eq. (12)], and the green line represents the $D = 0$ line. (d) The magnon bands in a ribbon geometry with 40 unit cells for $B = 0$ and (e) for $B = 0.05JS$. The colors of the bands represent the average vertical positions $\langle y \rangle$ of each mode along the axis where the sample is finite. The inset in (d) zooms in the trivial edge modes. For (a) and (b) and (d) and (e), the parameters $K = D = 0.2J$, $\phi'd = 0.2$, and $\theta_{\text{inc}} = 0$ are used.

results in topologically nontrivial phases with the Chern numbers $\text{sgn}(DB)$ for the upper magnon band [23]. The second component proportional to $(\phi'd)^3$ is a sublattice-symmetry-breaking mass that acts as a staggered onsite potential. The Haldane mass and the sublattice-symmetry-breaking mass compete to determine whether the phase is topologically trivial or not. Since the sublattice-symmetry-breaking mass depends on the spin chirality ϕ' injected from the boundaries, we can nonlocally manipulate the topological phase from the boundaries by controlling charge currents in heavy metals.

The topological phase of our system can be specified by the Chern numbers defined by $C^\pm = (1/2\pi) \int_{\text{BZ}} d^2k \Omega_z^\pm$ where $\Omega_z^\pm(\mathbf{k}) = \mp \frac{1}{2} \hat{\mathbf{n}} \cdot (\partial_{k_x} \hat{\mathbf{n}} \times \partial_{k_y} \hat{\mathbf{n}})$ is the Berry curvature of each magnon band and $\hat{\mathbf{n}}(\mathbf{k}) = \mathbf{h}(\mathbf{k})/|\mathbf{h}(\mathbf{k})|$. Figures 2(a) and 2(b) show the Berry curvature of the upper magnon band for the incident angle $\theta_{\text{inc}} = 0$ for two different values of B . When the external field is below the critical value (determined by the spin chirality) $|B| < |B_c|$ [see Fig. 2(a)], the Chern number C^+ for the upper band is zero. On the other hand, for the external field exceeding the critical value, the Chern number becomes $C^+ = +1$ for $B > |B_c|$ [see Fig. 2(b)] and -1 for

$B < -|B_c|$. Figure 2(c) summarizes the topological phases of our system. The phase diagram is truncated at $\phi'd = \pm 0.2$, which is below the Landau criterion for the spin chirality (for the used parameters) over which the static steady state becomes unstable [34].

A nontrivial band topology in bulk is followed by the existence of chiral edge modes according to the bulk-boundary correspondence [2]. Figures 2(d) and 2(e) plot the magnon bands at a ribbon geometry for the magnetic fields corresponding to Fig. 2(a) and 2(b) [40]. We can see that the localized edge modes in Fig. 2(d) can be deformed smoothly into bulk bands, while that in Fig. 2(c) bridge the gap and hence are chiral. The change of the magnon topology driven by the spin chirality ϕ' injected from the boundary constitutes one of our main results. Here, we remark that the effect of the spin chirality on the topological properties of magnon bands depends on the incident angle θ_{inc} through the sublattice-symmetry-breaking mass term $\propto (\phi'd)^3 \cos \theta_{\text{inc}}$ in Eq. (11). In particular, when $\theta_{\text{inc}} = \pm\pi/6$, the sublattice-symmetry-breaking mass term is absent in the magnon Dirac Hamiltonian and thus the magnon band's Chern numbers remain finite regardless of the injected spin chirality.

V. THERMAL HALL EFFECT

Our theoretical prediction of the chirality-induced topological phase transition can be experimentally examined by measuring the magnon thermal Hall conductivity, which can be expressed in terms of the Berry curvatures Ω_z^\pm [26,41]:

$$\kappa_{xy} = -\frac{k_B^2 T}{\hbar} \sum_{n=\pm} \int \frac{d^2\mathbf{k}}{(2\pi)^2} c_2(\rho_{n,\mathbf{k}}) \Omega_z^n(\mathbf{k}), \quad (13)$$

where $\rho_{n,\mathbf{k}} = (e^{E_{n,\mathbf{k}}/k_B T} - 1)^{-1}$ is the Bose-Einstein distribution function, $c_2(\rho) = (1 + \rho)[\ln[(1 + \rho)/\rho]]^2 - (\ln \rho)^2 - 2 \text{Li}_2(-\rho)$ and $\text{Li}_2(z)$ is the polylogarithm function. To estimate the thermal Hall conductivity numerically, we adopt the following material parameters for CrCl_3 . We assume $S = \frac{3}{2}$, which is a Cr magnetic moment of bulk chromium trihalides [42]. The exchange and the easy-plane anisotropy coefficients are given by $J = 0.79$ meV and $K = 0.03$ meV [27], which gives $K/J \approx 0.04$. For the DM interaction, we use $D = 0.2$ meV [43]. We choose $B = 2.2$ Oe for the external magnetic field. With the given parameters, Fig. 3 plots the thermal Hall conductivity κ_{xy} at $T = 10$ K as a function of the spin chirality ϕ' . For the small spin chirality $\phi'd \lesssim 0.06$, the thermal Hall conductivity κ_{xy} increases as the spin chirality ϕ' increases because of two reasons. First, the constant energy term h_0 [Eq. (8)] decreases as the spin chirality increases. This lowers the energy level at Dirac points and $c_2(\rho)$ increases accordingly. Second, the small spin-chirality-induced gap [the second term in Eq. (11)] broadens the gap width so that a broader region near the Dirac points contributes to $\Omega_z^n(\mathbf{k})$. When $\theta_{\text{inc}} \neq \pm\pi/6$, the profile of the thermal Hall conductivity develops a “shoulder” as we pass through the topological phase transition [Eq. (12)]. These shoulders appear at the phase boundary when the Chern number changes from ± 1 to 0 and therefore there arises the significant cancellation of the Berry-curvature contribution in the momentum-space

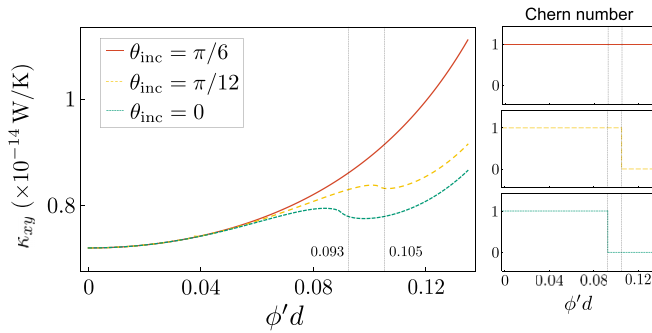


FIG. 3. Thermal Hall conductivity κ_{xy} as a function of the injected spin chirality ϕ' , where d is the lattice constant. The “shoulders” appear at the topological phase transition [Eq. (12)] for the incident angle $\theta_{\text{inc}} = 0$ and $\pi/12$. For the incident angle $\theta_{\text{inc}} = \pi/6$, there is no topological phase transition and thus no “shoulders” pattern in the thermal Hall conductivity. The plots on the right panel show the Chern numbers of the upper band as a function of the spin chirality. The used parameters are given in the main text.

integral in Eq. (13) [44]. Away from the phase boundary, the thermal Hall conductivity begins to increase again. When $\theta_{\text{inc}} = \pm\pi/6$ for which no topological phase transition occurs, the Chern number does not change and hence there is no “shoulder” pattern in the thermal Hall conductivity. Detecting the “shoulder” patterns in the profile of κ_{xy} can provide the feasibility of the suggested manipulation of magnonic topological phases. For a discussion about the temperature dependence of the “shoulder” pattern, see Appendix A 6.

VI. DISCUSSIONS

In this paper, we have investigated the manipulation of the magnon topology of honeycomb ferromagnets via the interfacial chirality injection. We have shown that the bulk magnon topology of the magnets can be electronically manipulated by inducing the spin chirality from the boundaries through the charge currents in the proximate heavy metals. As an experimental probe of the predicted chirality-induced topological phase transition of magnons, we have proposed the shoulderlike feature of the magnon thermal Hall conductivity.

While our proposed scheme to control a magnon topology by injecting a chirality is expected to work for generic easy-plane spin systems that host topological magnons and allow a spin current to flow in the form of a chiral spin texture, it would not work for easy-axis magnets due to the inertness of their uniform ground state to a spin-current injection. Also, here, we have focused on spin systems with sufficiently large S such that magnons defined by the truncated Holstein-Primakoff transformation are well defined. It is an open question whether the proposed scheme would work for quantum spin systems with small spin length S such as spin- $\frac{1}{2}$ systems.

We remark that the predicted topological phase transition occurs also in a honeycomb antiferromagnet whose Hamiltonian is given by Eq. (1) with $-J$ replaced by $J > 0$. Analogous to the ferromagnetic case, the spin chirality can be injected into the antiferromagnet by sandwiching it with heavy metals and flowing parallel currents through the heavy metals

[21,45]. It can be shown that the injected spin chirality can drive a topological phase transition of magnons in antiferromagnetic honeycombs subjected to an external field. The detailed discussion of the antiferromagnetic case is in Appendix B. Our scheme for the electronic control of magnon topology through boundary can be tested in 2D magnets with in-plane ordering, which includes ferromagnets CrCl_3 , $\text{Mn}_2\text{I}_3\text{Br}_3$ [46], and $\text{Cr}(\text{I}, \text{Cl})_3$ Janus monolayers [47] and antiferromagnets NiPS_3 [48] and MnPSe_3 [49]. Real materials at finite temperatures are expected to have impurities, in-plane anisotropies (associated with the crystal structure), and thermal fluctuations, which can disturb the formation of spin chiral textures. Although it has been shown that, if the injected spin current is sufficiently large to overcome the anisotropy, the spin chiral structures can be formed even in the presence of the in-plane anisotropies [50], the detailed investigation of their effects on the spin-chirality formation and suitable length scales for samples requires the comprehensive analytical and numerical studies, which is beyond the scope of this work. Our results indicate that the interfacial chirality injection might serve as versatile nonintrusive means to control the static and dynamical bulk properties of generic magnetic systems.

ACKNOWLEDGMENTS

We acknowledge the useful discussion with Y. Tserkovnyak. We also thank anonymous referees who helped us improve the manuscript, in particular concerning our experimental proposal. This work was supported by Brain Pool Plus Program through the National Research Foundation of Korea funded by the Ministry of Science and ICT (Grant No. NRF-2020H1D3A2A03099291), by the National Research Foundation of Korea (NRF) grant funded by the Korea government(MSIT) (Grant No. NRF-2021R1C1C1006273), and by the National Research Foundation of Korea funded by the Korea Government via the SRC Center for Quantum Coherence in Condensed Matter (Grant No. NRF-2016R1A5A1008184). G.G. was supported by the National Research Foundation of Korea (Grant No. NRF-2022R1C1C2006578).

APPENDIX A: HONEYCOMB FERROMAGNET

1. Derivation of continuum Hamiltonian

Consider a honeycomb ferromagnet on a honeycomb lattice whose Hamiltonian is given by Eq. (1). The vectors connecting the nearest-neighbor and the next-nearest-neighbor sites are given as follows [see Fig. 1(a)]:

$$\begin{aligned}\alpha_1 &= \frac{d}{2}(\sqrt{3}, 1), & \beta_1 &= \frac{\sqrt{3}d}{2}(1, -\sqrt{3}), \\ \alpha_2 &= \frac{d}{2}(-\sqrt{3}, 1), & \beta_2 &= \frac{\sqrt{3}d}{2}(1, \sqrt{3}), \\ \alpha_3 &= d(0, -1), & \beta_3 &= \sqrt{3}d(-1, 0).\end{aligned}\quad (\text{A1})$$

Let $\mathbf{S}_i = S\mathbf{m}_i$ and $A = 3\sqrt{3}d^2/2$ be the area of the unit cell. A continuum Hamiltonian of the model can be derived using

$\mathbf{m}_i - \mathbf{m}_j \simeq \nabla \mathbf{m} \cdot (\mathbf{r}_i - \mathbf{r}_j)$. Each term in Eq. (1) becomes as follows (up to some constant) in the continuum description:

$$H_{\text{Ex}} = JS^2 \sum_{(i,j)} (\mathbf{m}_i - \mathbf{m}_j)^2 \simeq \frac{A}{2} \int dx dy (\nabla \mathbf{m})^2, \quad (\text{A2})$$

$$H_{\text{EP}} = \frac{KS^2}{2} \sum_i m_{i,z}^2 \simeq \frac{\mathcal{K}}{2} \int dx dy m_z^2, \quad (\text{A3})$$

$$H_{\text{Zeeman}} = -BS \sum_i m_{i,z} \simeq -\mathcal{B} \int dx dy m_z, \quad (\text{A4})$$

where $\mathcal{A} = 2\sqrt{3}JS^2/3$, $\mathcal{K} = 4\sqrt{3}KS^2/9d^2$, and $\mathcal{B} = 4\sqrt{3}BS/9d^2$. Meanwhile, the DM interaction term does not contribute to the low-energy classical Hamiltonian. Treating the components of \mathbf{m}_i as a classical variable, $\hat{z} \cdot (\mathbf{m}_i \times \mathbf{m}_{i+\beta_j}) \simeq m_{i,x}(\nabla m_{i,y} \cdot \beta_j) - m_{i,y}(\nabla m_{i,x} \cdot \beta_j)$. Since $\sum_{j=1}^3 \beta_j = 0$, we get $\hat{z} \cdot \sum_{j=1}^3 (\mathbf{m}_i \times \mathbf{m}_{i+\beta_j}) = 0$ and hence

$$\begin{aligned} H_{\text{DMI}} &= DS^2 \hat{z} \cdot \sum_{j=1}^3 \left(\sum_{i \in A} \mathbf{m}_i \times \mathbf{m}_{i+\beta_j} - \sum_{i \in B} \mathbf{m}_i \times \mathbf{m}_{i+\beta_j} \right) \\ &= 0. \end{aligned} \quad (\text{A5})$$

Combining Eqs. (A2)–(A5), the continuum Hamiltonian density for the honeycomb ferromagnet becomes

$$\mathcal{H} = \frac{\mathcal{A}}{2} (\nabla \mathbf{m})^2 + \frac{\mathcal{K}}{2} m_z^2 - \mathcal{B} m_z. \quad (\text{A6})$$

2. Spin chirality injection

The classical spin dynamics is described by the Landau-Lifshitz-Gilbert (LLG) equation

$$\begin{aligned} \dot{\mathbf{m}} + \alpha \mathbf{m} \times \dot{\mathbf{m}} &= -s^{-1} \mathbf{m} \times \frac{\partial H}{\partial \mathbf{m}} \\ &= -s^{-1} \mathbf{m} \times (-A \nabla^2 \mathbf{m} + \mathcal{K} m_z \hat{z} - \mathcal{B} \hat{z}), \end{aligned} \quad (\text{A7})$$

where s is a local spin density. In the spherical coordinates, $\mathbf{m} = (\sin \theta \cos \phi, \sin \theta \sin \phi, \cos \theta) \in S^2$ and

$$\begin{aligned} \dot{\mathbf{m}} &= \dot{\theta} \hat{\theta} + (\dot{\phi} \sin \theta) \hat{\phi}, \\ \partial_a \mathbf{m} &= (\partial_a \theta) \hat{\theta} + (\partial_a \phi \sin \theta) \hat{\phi}, \\ \partial_a^2 \mathbf{m} &= -(\partial_a^2 \theta + \sin^2 \theta \partial_a^2 \phi) \mathbf{m} + (\partial_a^2 \theta - \sin \theta \cos \theta \partial_a^2 \phi) \hat{\theta} \\ &\quad + (\sin \theta \partial_a^2 \phi + 2 \cos \theta \partial_a \theta \partial_a \phi) \hat{\phi}, \\ m_z \hat{z} &= \cos \theta (\cos \theta \mathbf{m} + \sin \theta \hat{\theta}), \end{aligned} \quad (\text{A8})$$

for $a = x, y$. Here the ordered set $\{\mathbf{m}, \hat{\theta}, \hat{\phi}\}$ forms a right-handed coordinate system. Substituting Eqs. (A8) into Eq. (A7),

$$\begin{aligned} -s \sin \theta \dot{\phi} - \alpha s \dot{\theta} &= -A \nabla^2 \theta - \mathcal{A} \sin \theta \cos \theta \sum_{a=x,y} (\partial_a \phi)^2 \\ &\quad - \mathcal{K} \sin \theta \cos \theta + \mathcal{B} \sin \theta, \end{aligned} \quad (\text{A9})$$

$$s \dot{\theta} - \alpha s \sin \theta \dot{\phi} = -\mathcal{A} \left[2 \cos \theta \sum_{a=x,y} \partial_a \theta \partial_a \phi + \sin \theta \nabla^2 \phi \right]. \quad (\text{A10})$$

Multiplying both sides of Eq. (A10) by $\sin \theta$, we get (assuming $\alpha = 0$)

$$-\partial_t (s \cos \theta) = -\mathcal{A} \sum_{a=x,y} \partial_a (\sin^2 \theta \partial_a \phi), \quad (\text{A11})$$

which is the continuity equation $\partial_t (s m_z) + \nabla \cdot \mathbf{J}_z^s = 0$ for the spin density $s m_z = s \cos \theta$ and the spin-current density $\mathbf{J}_z^s = -\mathcal{A} \sin^2 \theta \nabla \phi$.

Let us consider a steady-state solution with an ansatz $\theta(\mathbf{r}, t) = \theta_0$ and $\phi(\mathbf{r}, t) = \phi(x, t)$ [see Fig. 1(b)]. From Eqs. (A9) and (A10),

$$\dot{\phi} = \frac{\mathcal{A} (\partial_x \phi)^2 \cos \theta_0 + \mathcal{K} \cos \theta_0 - \mathcal{B}}{s} \equiv \Omega, \quad (\text{A12})$$

$$\phi'(x) = \frac{\alpha s}{\mathcal{A} \sin \theta_0} \Omega x + \phi'(0), \quad (\text{A13})$$

which lead to $\phi(\mathbf{r}, t) = \phi(x) + \Omega t$. When the sample is sandwiched between the heavy metals with charge currents $j_{L/R}$ flowing on them, the spin-current injection occurs at the interfaces and the related boundary conditions are given by [22]

$$(J_{L/R}^s)_z = \sin^2 \theta_0 (j_{L/R} \vartheta \mp \gamma_{L/R} \Omega), \quad (\text{A14})$$

where ϑ is the dampinglike torque coefficient and $\gamma_{L/R}$ is the renormalized spin-mixing conductance. We then obtain two expressions for the loss of spin current $\Delta J_z^s \equiv (J_L^s)_z - (J_R^s)_z$:

$$\Delta J_z^s = \sin^2 \theta_0 [(j_L - j_R) \vartheta - (\gamma_L + \gamma_R) \Omega], \quad (\text{A15})$$

$$\Delta J_z^s = -\mathcal{A} \sin^2 \theta_0 \left(-\frac{\alpha s}{\mathcal{A} \sin \theta_0} \Omega L \right) = \alpha s \Omega L \sin \theta_0. \quad (\text{A16})$$

Equating Eqs. (A15) and (A16), we get

$$\Omega = \frac{(j_L - j_R) \vartheta}{2\gamma + \alpha s L / \sin \theta_0}. \quad (\text{A17})$$

Therefore, for a series configuration $j_L = j_R$, we have $\Omega = 0$. Then, $(J_L^s)_z = -\mathcal{A} \sin^2 \theta_0 \phi' = \sin^2 \theta_0 j \vartheta$ and hence the system has a static spiraling spin texture with $\phi' = -j \vartheta / \mathcal{A}$.

3. Equilibrium angle of the ground state

Define the angle of incidence θ_{inc} of the spin superfluid on the honeycomb lattice as shown in Fig. 1(b) ($-\pi/6 \leq \theta_{\text{inc}} \leq \pi/6$). The spin current flows along the x' direction. Assume the static spiral spin texture as discussed in Appendix A 2. Define the azimuthal angle field $\phi(\mathbf{r})$ on the honeycomb lattice. Since $\nabla' \phi = (\phi', 0)$ where $\phi' \equiv \partial \phi / \partial x'$ and

$$\begin{pmatrix} x' \\ y' \end{pmatrix} = \begin{pmatrix} \cos \theta_{\text{inc}} & -\sin \theta_{\text{inc}} \\ \sin \theta_{\text{inc}} & \cos \theta_{\text{inc}} \end{pmatrix} \begin{pmatrix} x \\ y \end{pmatrix}, \quad (\text{A18})$$

the gradient of ϕ in the (x, y) coordinates is $\nabla \phi = \phi' (\cos \theta_{\text{inc}}, -\sin \theta_{\text{inc}})$.

Let θ_0 be the equilibrium polar angle of the ground state and $\mathbf{S}_A(\phi)$ [$\mathbf{S}_B(\phi)$] be the spin in the A (B) sublattice with azimuthal angle ϕ . By definition, $\mathbf{S}_{A/B}(\phi) = S(\sin \theta_0 \cos \phi, \sin \theta_0 \sin \phi, \cos \theta_0)$. Then, for any ϕ_0 , we have

$$\begin{aligned} \mathbf{S}_A(\phi_0) \cdot \sum_{j=1}^3 \mathbf{S}_B(\phi_0 + \alpha_j \cdot \nabla \phi) \\ = S^2 [3 \cos^2 \theta_0 + \sin^2 \theta_0 g(\phi'd, \theta_{\text{inc}})], \end{aligned} \quad (\text{A19})$$

$$\begin{aligned} & \hat{z} \cdot \left[\mathbf{S}_{A/B}(\phi_0) \times \sum_{j=1}^3 \mathbf{S}_{A/B}(\phi_0 + \boldsymbol{\beta}_j \cdot \nabla \phi) \right] \\ & = S^2 \sin^2 \theta_0 h(\phi'd, \theta_{\text{inc}}), \end{aligned} \quad (\text{A20})$$

where $g(\phi'd, \theta_{\text{inc}}) \equiv \sum_{j=1}^3 \cos(\nabla \phi \cdot \boldsymbol{\alpha}_j)$ and $h(\phi'd, \theta_{\text{inc}}) \equiv \sum_{j=1}^3 \sin(\nabla \phi \cdot \boldsymbol{\beta}_j)$ ($\phi'd$ is the change in the azimuthal angle per the distance between neighboring sites in the x' direction). Let us denote the total number of sites on the lattice by N . Then, the exchange and the DMI terms become

$$H_{\text{Ex}} = -\frac{N}{2} JS^2 [3 \cos^2 \theta_0 + \sin^2 \theta_0 g(\phi'd, \theta_{\text{inc}})], \quad (\text{A21})$$

$$\begin{aligned} H_{\text{DMI}} &= \frac{N}{2} D [\text{Eq. (A20) for A}] - [\text{Eq. (A20) for B}] \\ &= 0. \end{aligned} \quad (\text{A22})$$

The easy-plane and the Zeeman terms are $H_{\text{EP}} = NKS^2 \cos^2 \theta_0 / 2$ and $H_{\text{Zeeman}} = -NBS \cos \theta_0$, respectively. Thus, the classical Hamiltonian of the honeycomb ferromagnet with spin chirality is given by

$$\begin{aligned} H_{\text{cl}} &= -\frac{NS}{2} [2B \cos \theta_0 + (3J - K)S \cos^2 \theta_0 \\ &+ JS \sin^2 \theta_0 g(\phi'd, \theta_{\text{inc}})]. \end{aligned} \quad (\text{A23})$$

The function g satisfies $g(\phi'd, \theta_{\text{inc}}) \leq 3$ for $(\phi'd, \theta_{\text{inc}}) \in [-\pi, \pi] \times [-\pi/6, \pi/6]$ and the equality holds only when $\phi'd = 0$.

Let $f \equiv 2H_{\text{cl}}/NS = -gJS - 2B \cos \theta_0 + K_{\text{eff}}S \cos^2 \theta_0$ where $K_{\text{eff}} = K - J(3 - g(\phi'd, \theta_{\text{inc}}))$. Note that when $\phi' = 0$, $f = -3JS - 2B \cos \theta_0 + KS \cos^2 \theta_0$. Thus, the effect of the finite chirality is reflected in the renormalized anisotropy K_{eff} , reducing the effect of the easy-plane anisotropy K slightly. Searching for the value of θ_0 satisfying $\partial f / \partial \theta_0 = 0$ and $\partial^2 f / \partial \theta_0^2 \geq 0$, one can conclude that the equilibrium angle θ_0

is determined by

$$\theta_0 = \Theta(K_{\text{eff}}S - |B|) \cos^{-1} \left(\frac{B}{K_{\text{eff}}S} \right), \quad (\text{A24})$$

where Θ is the Heaviside theta function. Note that when there is no magnetic field ($B = 0$), we obtain $\theta_0 = \pi/2$ regardless of the value of $\phi'd$.

4. Numerical justification for ignoring $\lambda(\mathbf{k})$

Figure 4 shows a numerical comparison between the magnon bands near the two Dirac points obtained from the approximated Hamiltonian with no pairing terms $\lambda(\mathbf{k})$ [Eqs. (8) and (9)] and the exact full Hamiltonian [Eqs. (4)–(7)]. Note that the approximated bands perfectly agree with the exact bands across the phase boundary [Eq. (12)]. This justifies using the approximated Hamiltonian to study the band topology.

5. Shifted Dirac points and Dirac Hamiltonians

The position of the shifted Dirac points $\bar{\mathbf{K}}$ and $\bar{\mathbf{K}}'$ can be obtained by looking for the zeros of the equation $\rho_j(\mathbf{k}, \nabla \phi) = 0$ where $\rho_j(\mathbf{k}, \nabla \phi) = e^{-i\mathbf{k} \cdot \boldsymbol{\alpha}_j} (\cos \frac{\varphi_{\alpha_j}}{2} - i \cos \theta_0 \sin \frac{\varphi_{\alpha_j}}{2})^2$ and $\varphi_{\alpha_j} = \nabla \phi \cdot \boldsymbol{\alpha}_j$. When $\phi' = 0$, the zeros are the original Dirac points $\mathbf{K} = (4\pi/3a, 0)$ and $\mathbf{K}' = (2\pi/3a, 2\pi/\sqrt{3}a)$. For nonzero ϕ' , solving $\rho_j(\mathbf{k}, \nabla \phi) = 0$ perturbatively up to the order of $(\phi'd)^3$ yields

$$\begin{aligned} (\bar{\mathbf{K}})_{k_x} &= \frac{4\pi}{3\sqrt{3}d} - \phi' \cos \theta_0 \cos \theta_{\text{inc}} + \frac{\phi'^2 d}{8} \sin^2 \theta_0 \cos 2\theta_{\text{inc}} \\ &- \frac{\phi'^3 d^2}{16} \cos \theta_0 \sin^2 \theta_0 \cos \theta_{\text{inc}}, \end{aligned} \quad (\text{A25})$$

$$\begin{aligned} (\bar{\mathbf{K}})_{k_y} &= \cos \theta_0 \sin \theta_{\text{inc}} + \frac{\phi'^2 d}{8} \sin^2 \theta_0 \sin 2\theta_{\text{inc}} \\ &+ \frac{\phi'^3 d^2}{16} \cos \theta_0 \sin^2 \theta_0 \sin \theta_{\text{inc}}, \end{aligned} \quad (\text{A26})$$

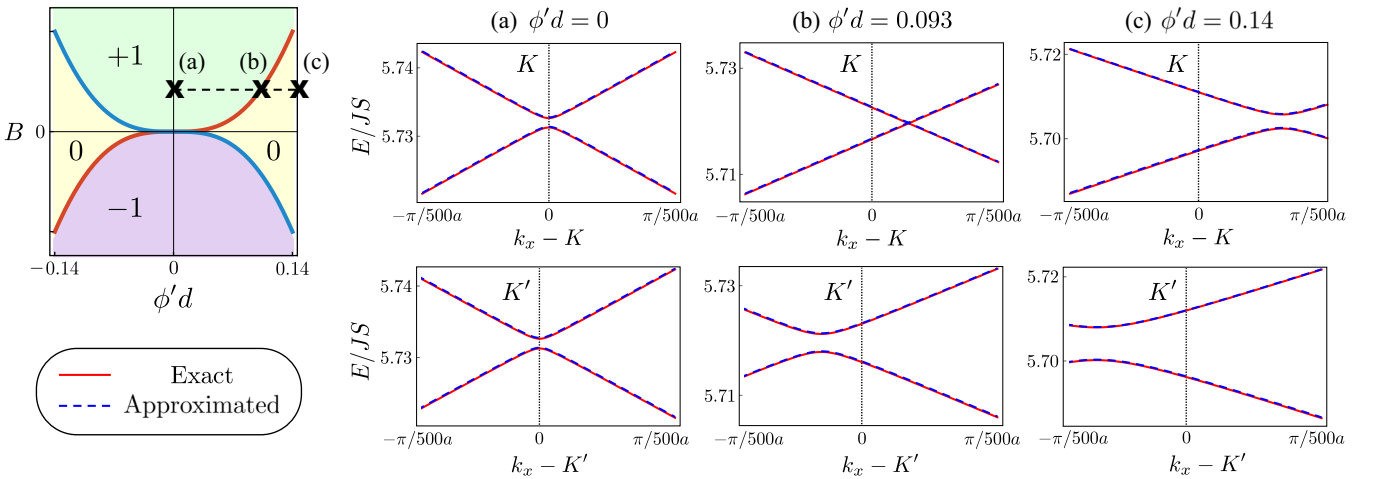


FIG. 4. Numerical comparison between the bands obtained from the exact Hamiltonian with magnon-pairing terms (red, solid) and the approximated Hamiltonian (blue, dashed) near the two Dirac points. (a) $\phi'd = 0$. (b) $\phi'd = 0.093$. Note that the approximated magnon bands correctly capture the gap closing at the phase boundary [Eq. (12)]. (c) $\phi'd = 0.14$. The parameters used are the same as those used in Fig. 3.

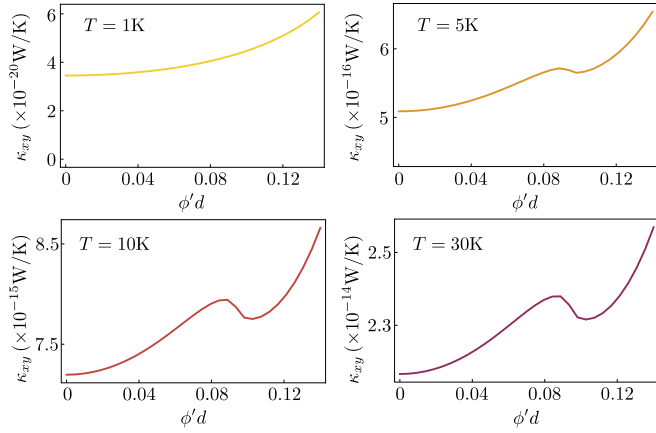


FIG. 5. Magnon thermal Hall conductivity κ_{xy} at various temperatures T for the case $\theta_{\text{inc}} = 0$.

$$(\bar{\mathbf{K}}')_{k_x} = \frac{2\pi}{3a} - \phi' \cos \theta_0 \cos \theta_{\text{inc}} - \frac{\phi'^2 d}{8} \sin^2 \theta_0 \cos 2\theta_{\text{inc}} - \frac{\phi'^3 d^2}{16} \cos \theta_0 \sin^2 \theta_0 \cos \theta_{\text{inc}}, \quad (\text{A27})$$

$$(\bar{\mathbf{K}}')_{k_y} = \frac{2\pi}{\sqrt{3}a} + \phi' \cos \theta_0 \sin \theta_{\text{inc}} - \frac{\phi'^2 d}{8} \sin^2 \theta_0 \sin 2\theta_{\text{inc}} + \frac{\phi'^3 d^2}{16} \cos \theta_0 \sin^2 \theta_0 \sin \theta_{\text{inc}}. \quad (\text{A28})$$

We can obtain a Dirac Hamiltonian near the shifted Dirac points by expanding $H = \sum_{\mathbf{k}} \Psi_{\mathbf{k}}^\dagger [h_0 I + \mathbf{h}(\mathbf{k}) \cdot \boldsymbol{\sigma}] \Psi_{\mathbf{k}}$ given in Eqs. (8) and (9) near $\bar{\mathbf{K}}$ and $\bar{\mathbf{K}}'$ given in Eqs. (A25)–(A28). Here we present the Dirac Hamiltonian for the case $\theta_{\text{inc}} = 0$ near $\bar{\mathbf{K}}$:

$$h_{\bar{\mathbf{K}},1}(\mathbf{p}) = \frac{3Jsd}{2} p_x + \frac{3J(B^2 - K^2 S^2) \phi'^2 d^3}{8K^2 S} p_x, \quad (\text{A29})$$

$$h_{\bar{\mathbf{K}},2}(\mathbf{p}) = -\frac{3Jsd}{2} p_y, \quad (\text{A30})$$

$$h_{\bar{\mathbf{K}},3}(\mathbf{p}) = -\frac{3\sqrt{3}BD}{K} + \frac{9\sqrt{3}D(B^2 - K^2 S^2) \phi'^2 d^2}{4K^2 S} p_x + \frac{9\sqrt{3}DB[B^2 p_x d + KS^2(4J - K p_x d)] \phi'^2 d^2}{16K^3 S^2} + \frac{3\sqrt{3}D}{64K^4 S^3} [B^4(9p_x d - 10) + K^4 S^4(15p_x d - 26) + 12B^2 K S^2 [6J p_x d + K(3 - 2p_x d)]], \quad (\text{A31})$$

where \mathbf{p} is a small momentum deviation from $\bar{\mathbf{K}}$. For general θ_{inc} , the third components (mass term) of the Dirac Hamiltonians at the shifted Dirac points ($\mathbf{p} = 0$) are given by

$$h_{\bar{\mathbf{K}}/\bar{\mathbf{K}}',3}(\mathbf{0}) = \frac{3\sqrt{3}D}{32K^4 S^3} [\pm 8BK^2 S^3 [4K + 3J(\phi' d)^2] + (-5B^4 + 18B^2 K^2 S^2 - 13K^4 S^4) \times (\phi' d)^3 \cos 3\theta_{\text{inc}}]. \quad (\text{A32})$$

The gap size Δ is twice the absolute value of Eq. (A32), which reduces to Eq. (11) for a small magnetic field B .

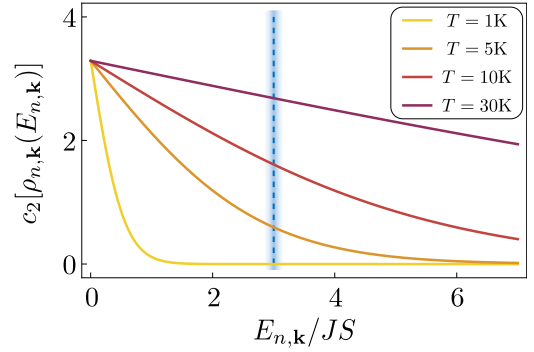


FIG. 6. $c_2[\rho_{n,\mathbf{k}}(E_{n,\mathbf{k}})]$ in Eq. (13) as a function of the magnon-band energy $E_{n,\mathbf{k}}/JS$ at various temperatures T . The blue dashed line indicates the energy values near the Dirac points.

6. Temperature dependence of the “shoulder” pattern

The “shoulder” persists for any temperatures sufficiently large enough so that enough population of thermal magnons exists near the Dirac points, where the Berry curvature takes nontrivial values. For the parameters used in Sec. V, the “shoulder” starts to be detectable near $T = 5$ K and continues to exist at higher temperatures (see Fig. 5). Figure 6 clearly displays that the function $c_2[\rho_{n,\mathbf{k}}(E_{n,\mathbf{k}})]$ inside the integration in Eq. (13) is largely suppressed at low temperatures ($T \simeq 1$ K) near the blue dashed line, which corresponds to energies $E_{n,\mathbf{k}}$ near the Dirac points where the Berry curvature $\Omega_{\mathbf{k}}^n$ is large. As temperature increases, the value of $c_2[\rho_{n,\mathbf{k}}(E_{n,\mathbf{k}})]$ near the blue dashed line increases and therefore the change of the Chern number from one to zero results in the shoulder-shaped profile of the magnon thermal Hall conductivity κ_{xy} . Note that there is a critical temperature T_c above which the magnetic order does not persist. Near and above T_c , our linear spin-wave approach is not well justified and therefore we expect that the temperature window to observe the “shoulder” from κ_{xy} will be bounded above by some fraction of T_c .

APPENDIX B: HONEYCOMB ANTIFERROMAGNET

1. Model and ground state

Consider a honeycomb antiferromagnet on a honeycomb lattice whose Hamiltonian is given by

$$H = J \sum_{\langle i,j \rangle} \mathbf{S}_i \cdot \mathbf{S}_j + \frac{K}{2} \sum_i S_{i,z}^2 + D \sum_{\langle\langle i,j \rangle\rangle} v_{ij} \hat{\mathbf{z}} \cdot (\mathbf{S}_i \times \mathbf{S}_j) - B \sum_i S_{i,z}. \quad (\text{B1})$$

All terms in Eq. (B1) are the same as the ferromagnetic model in Eq. (1), except for the sign of the exchange term. We again consider a setup shown in Fig. 1(b) to inject spin chirality into the antiferromagnet. Let θ_A (θ_B) be the ground-state equilibrium polar angle of the spins belonging to the sublattice A (B). Let $\mathbf{S}_{A/B}(\phi)$ denote a spin in the sublattice A (B) with azimuthal angle ϕ , whose components in the Cartesian coordinates are given by $\mathbf{S}_{A/B}(\phi) = S(\sin \theta_{A/B} \cos \phi, \sin \theta_{A/B} \sin \phi, \cos \theta_{A/B})$. Then, for any ϕ_0 , we

obtain

$$\begin{aligned} \mathbf{S}_A(\phi_0) \cdot \sum_{j=1}^3 \mathbf{S}_B(\phi_0 + \boldsymbol{\alpha}_j \cdot \nabla \phi) \\ = S^2 [3 \cos \theta_A \cos \theta_B + \sin \theta_A \sin \theta_B g(\phi'd, \theta_{\text{inc}})], \end{aligned} \quad (\text{B2})$$

$$\begin{aligned} \hat{z} \cdot \left[\mathbf{S}_{A/B}(\phi_0) \times \sum_{j=1}^3 \mathbf{S}_{A/B}(\phi_0 + \boldsymbol{\beta}_j \cdot \nabla \phi) \right] \\ = S^2 \sin^2 \theta_{A/B} h(\phi'd, \theta_{\text{inc}}). \end{aligned} \quad (\text{B3})$$

Denoting the total number of sites on each sublattice by N , the easy-plane and the Zeeman terms of Eq. (B1) become $H_{\text{EP}} = NKS^2(\cos^2 \theta_A + \cos^2 \theta_B)/2$ and $H_{\text{Zeeman}} = -NBS(\cos \theta_A + \cos \theta_B)$. Then, the classical Hamiltonian of the honeycomb antiferromagnet with spin chirality becomes

$$\begin{aligned} H_{\text{cl}} = \frac{NS}{2} [KS(\cos^2 \theta_A + \cos^2 \theta_B) - 2B(\cos \theta_A + \cos \theta_B) \\ + 2JS[3 \cos \theta_A \cos \theta_B + \sin \theta_A \sin \theta_B g(\phi'd, \theta_{\text{inc}})] \\ + 2DS h(\phi'd, \theta_{\text{inc}})(\sin^2 \theta_A - \sin^2 \theta_B)]. \end{aligned} \quad (\text{B4})$$

We can obtain the equilibrium polar angles θ_A and θ_B by looking for the arguments that minimize H_{cl} .

2. Magnon Hamiltonian

As in Sec. III for the ferromagnetic model, by performing local spin rotations, the Holstein-Primakoff transformation, and the Fourier transformation sequentially, we can again obtain the magnon Hamiltonian in the momentum space. Note that for the antiferromagnetic model we should rotate spins

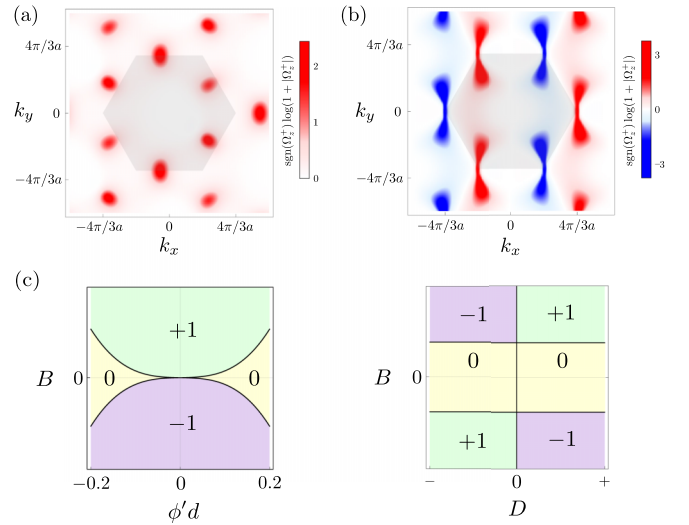


FIG. 7. (a) The Berry curvature Ω_z^+ of the upper magnon band in a honeycomb antiferromagnet under chirality injection for $B = 1.8JS$ and (b) for $B = 0$. (c) The topological phase diagram for antiferromagnet. For (a) and (b), the parameters $K = D = 0.2J$, $\phi'd = 0.2$, and $\theta_{\text{inc}} = 0$ are used.

in different sublattices with different polar angles θ_A and θ_B . Introducing the Nambu spinor $\psi_{\mathbf{k}} = (a_{\mathbf{k}}, b_{\mathbf{k}}, a_{-\mathbf{k}}^\dagger, b_{-\mathbf{k}}^\dagger)^T$, the magnon Hamiltonian of the honeycomb antiferromagnet can be written as $H = \frac{1}{2} \sum_{\mathbf{k}} \psi_{\mathbf{k}}^\dagger \mathcal{H}(\mathbf{k}) \psi_{\mathbf{k}}$ with

$$\mathcal{H}_{\mathbf{k}} = \begin{pmatrix} h(\mathbf{k}) & \lambda(\mathbf{k}) \\ \lambda(\mathbf{k})^\dagger & h(-\mathbf{k})^T \end{pmatrix}, \quad (\text{B5})$$

where

$$h(\mathbf{k}) = \begin{pmatrix} \epsilon_A & 0 \\ 0 & \epsilon_B \end{pmatrix} + S \sum_{j=1}^3 \begin{pmatrix} -J \sin \theta_A \sin \theta_B \cos \varphi_{\alpha_j} + D f_{A,j}(\mathbf{k}, \nabla \phi) & J \gamma_j(\mathbf{k}, \nabla \phi) \\ J \gamma_j^*(\mathbf{k}, \nabla \phi) & -J \sin \theta_A \sin \theta_B \cos \varphi_{\alpha_j} - D f_{B,j}(\mathbf{k}, \nabla \phi) \end{pmatrix}, \quad (\text{B6})$$

$$\lambda(\mathbf{k}) = \frac{1}{2} KS \begin{pmatrix} \sin^2 \theta_A & 0 \\ 0 & \sin^2 \theta_B \end{pmatrix} + S \sum_{j=1}^3 \begin{pmatrix} -D \sin^2 \theta_A e^{-i\mathbf{k} \cdot \boldsymbol{\beta}_j} \sin \varphi_{\beta_j} & J \tilde{\gamma}_j(\mathbf{k}, \nabla \phi) \\ J \tilde{\gamma}_j(-\mathbf{k}, \nabla \phi) & D \sin^2 \theta_B e^{-i\mathbf{k} \cdot \boldsymbol{\beta}_j} \sin \varphi_{\beta_j} \end{pmatrix}, \quad (\text{B7})$$

$$\epsilon_{A/B} = B \cos \theta_{A/B} - \frac{1}{4} KS(1 + 3 \cos 2\theta_{A/B}) - 3JS \cos \theta_A \cos \theta_B, \quad (\text{B8})$$

$$f_{A/B,j}(\mathbf{k}, \nabla \phi) = (3 + \cos 2\theta_{A/B}) \cos(\mathbf{k} \cdot \boldsymbol{\beta}_j) \sin \varphi_{\beta_j} - 4 \sin^2 \theta_{A/B} \sin \varphi_{\beta_j} + 4 \cos \theta_{A/B} \sin(\mathbf{k} \cdot \boldsymbol{\beta}_j) \cos \varphi_{\beta_j}, \quad (\text{B9})$$

$$\gamma_j(\mathbf{k}, \nabla \phi) = e^{i\mathbf{k} \cdot \boldsymbol{\alpha}_j} [\sin \theta_A \sin \theta_B + (1 + \cos \theta_A \cos \theta_B) \cos \varphi_{\alpha_j} + i(\cos \theta_A + \cos \theta_B) \sin \varphi_{\alpha_j}], \quad (\text{B10})$$

$$\tilde{\gamma}_j(\mathbf{k}, \nabla \phi) = e^{i\mathbf{k} \cdot \boldsymbol{\alpha}_j} [\sin \theta_A \sin \theta_B - (1 - \cos \theta_A \cos \theta_B) \cos \varphi_{\alpha_j} - i(\cos \theta_A - \cos \theta_B) \sin \varphi_{\alpha_j}]. \quad (\text{B11})$$

3. Topological phase transition

We can analyze the topological phases of the antiferromagnet under chirality injection by calculating the Chern numbers of the magnon bands via the scheme of Fukui *et al.* [51]. Figures 7(a) and 7(b) show the Berry curvatures of the upper magnon band of the Hamiltonian given by Eqs. (B5)–(B11). Under a magnetic field that yields a noncollinear (canted) Neel

order, the Berry curvature has the same sign all over the first Brillouin zone as shown in Fig. 7(a) with the corresponding Chern number +1, which is consistent with the previous study [52]. Meanwhile, when $B = 0$, the effective time-reversal symmetry is restored and the Berry curvature sums up to vanish [see Fig. 7(b)], resulting in a topologically trivial phase. Figure 7(c) shows the chirality-induced topological phase diagram of the antiferromagnet. The overall feature of

the topological phase transition of the antiferromagnet is analogous to that of the ferromagnet. We numerically

checked that the trivial phase disappears when $\theta_{\text{inc}} = \pm\pi/6$ as the ferromagnets.

-
- [1] K. v. Klitzing, G. Dorda, and M. Pepper, *Phys. Rev. Lett.* **45**, 494 (1980).
- [2] M. Z. Hasan and C. L. Kane, *Rev. Mod. Phys.* **82**, 3045 (2010).
- [3] X.-L. Qi and S.-C. Zhang, *Rev. Mod. Phys.* **83**, 1057 (2011).
- [4] F. D. M. Haldane, *Phys. Rev. Lett.* **61**, 2015 (1988).
- [5] B. A. Bernevig and S.-C. Zhang, *Phys. Rev. Lett.* **96**, 106802 (2006).
- [6] Y. L. Chen, J. G. Analytis, J.-H. Chu, Z. K. Liu, S.-K. Mo, X. L. Qi, H. J. Zhang, D. H. Lu, X. Dai, Z. Fang, S. C. Zhang, I. R. Fisher, Z. Hussain, and Z.-X. Shen, *Science* **325**, 178 (2009).
- [7] A. R. Mellnik, J. S. Lee, A. Richardella, J. L. Grab, P. J. Mintun, M. H. Fischer, A. Vaezi, A. Manchon, E.-A. Kim, N. Samarth, and D. C. Ralph, *Nature (London)* **511**, 449 (2014).
- [8] Y. Fan, P. Upadhyaya, X. Kou, M. Lang, S. Takei, Z. Wang, J. Tang, L. He, L.-T. Chang, M. Montazeri, G. Yu, W. Jiang, T. Nie, R. N. Schwartz, Y. Tserkovnyak, and K. L. Wang, *Nat. Mater.* **13**, 699 (2014).
- [9] Y. Wang, P. Deorani, K. Banerjee, N. Koirala, M. Brahlek, S. Oh, and H. Yang, *Phys. Rev. Lett.* **114**, 257202 (2015).
- [10] Y. Wang, D. Zhu, Y. Wu, Y. Yang, J. Yu, R. Ramaswamy, R. Mishra, S. Shi, M. Elyasi, K.-L. Teo, Y. Wu, and H. Yang, *Nat. Commun.* **8** (2017).
- [11] L. Zhang, J. Ren, J.-S. Wang, and B. Li, *Phys. Rev. B* **87**, 144101 (2013).
- [12] R. Shindou, R. Matsumoto, S. Murakami, and J.-i. Ohe, *Phys. Rev. B* **87**, 174427 (2013).
- [13] A. Mook, J. Henk, and I. Mertig, *Phys. Rev. B* **89**, 134409 (2014).
- [14] A. Mook, J. Henk, and I. Mertig, *Phys. Rev. B* **90**, 024412 (2014).
- [15] X. S. Wang and X. R. Wang, *J. Appl. Phys.* **129**, 151101 (2021).
- [16] Y.-S. Lu, J.-L. Li, and C.-T. Wu, *Phys. Rev. Lett.* **127**, 217202 (2021).
- [17] A. Mook, K. Plekhanov, J. Klinovaja, and D. Loss, *Phys. Rev. X* **11**, 021061 (2021).
- [18] G. Go, S. K. Kim, and K.-J. Lee, *Phys. Rev. Lett.* **123**, 237207 (2019).
- [19] S. K. Kim, K. Nakata, D. Loss, and Y. Tserkovnyak, *Phys. Rev. Lett.* **122**, 057204 (2019).
- [20] S. Takei and Y. Tserkovnyak, *Phys. Rev. Lett.* **112**, 227201 (2014).
- [21] S. Takei, B. I. Halperin, A. Yacoby, and Y. Tserkovnyak, *Phys. Rev. B* **90**, 094408 (2014).
- [22] S. Takei and Y. Tserkovnyak, *Phys. Rev. Lett.* **115**, 156604 (2015).
- [23] S. K. Kim, H. Ochoa, R. Zarzuela, and Y. Tserkovnyak, *Phys. Rev. Lett.* **117**, 227201 (2016).
- [24] S. A. Owerre, *J. Phys.: Condens. Matter* **28**, 386001 (2016).
- [25] S. A. Owerre, *J. Appl. Phys.* **120**, 043903 (2016).
- [26] R. Matsumoto and S. Murakami, *Phys. Rev. Lett.* **106**, 197202 (2011).
- [27] X. Lu, R. Fei, L. Zhu, and L. Yang, *Nat. Commun.* **11**, 4724 (2020).
- [28] F. Xue, Y. Hou, Z. Wang, and R. Wu, *Phys. Rev. B* **100**, 224429 (2019).
- [29] M. Dupont, Y. O. Kvashnin, M. Shiranzaei, J. Fransson, N. Laflorencie, and A. Kantian, *Phys. Rev. Lett.* **127**, 037204 (2021).
- [30] I. Dzyaloshinsky, *J. Phys. Chem. Solids* **4**, 241 (1958).
- [31] Y. O. Kvashnin, A. Bergman, A. I. Lichtenstein, and M. I. Katsnelson, *Phys. Rev. B* **102**, 115162 (2020).
- [32] E. B. Sonin, *Zh. Eksp. Teor. Fiz.* **74**, 2097 (1978) [*Sov. Phys.-JETP* **47**, 1091 (1978)].
- [33] J. König, M. C. Bønsager, and A. H. MacDonald, *Phys. Rev. Lett.* **87**, 187202 (2001).
- [34] E. Sonin, *Adv. Phys.* **59**, 181 (2010).
- [35] J. Sinova, S. O. Valenzuela, J. Wunderlich, C. H. Back, and T. Jungwirth, *Rev. Mod. Phys.* **87**, 1213 (2015).
- [36] A. Manchon, J. Železný, I. M. Miron, T. Jungwirth, J. Sinova, A. Thiaville, K. Garello, and P. Gambardella, *Rev. Mod. Phys.* **91**, 035004 (2019).
- [37] Y. Tserkovnyak and S. A. Bender, *Phys. Rev. B* **90**, 014428 (2014).
- [38] T. Holstein and H. Primakoff, *Phys. Rev.* **58**, 1098 (1940).
- [39] G. Chaudhary, M. Levin, and A. A. Clerk, *Phys. Rev. B* **103**, 214306 (2021).
- [40] When obtaining the edge state, the onsite potential is added at the outermost sites such that the onsite potential is uniform in the system [53,54].
- [41] S. Murakami and A. Okamoto, *J. Phys. Soc. Jpn.* **86**, 011010 (2017).
- [42] J. F. Dillon and C. E. Olson, *J. Appl. Phys.* **36**, 1259 (1965).
- [43] Z. Cai, S. Bao, Z.-L. Gu, Y.-P. Gao, Z. Ma, Y. Shangguan, W. Si, Z.-Y. Dong, W. Wang, Y. Wu, D. Lin, J. Wang, K. Ran, S. Li, D. Adroja, X. Xi, S.-L. Yu, X. Wu, J.-X. Li, and J. Wen, *Phys. Rev. B* **104**, L020402 (2021).
- [44] While the appearance of the “shoulder” pattern upon the decrease of the Chern number is numerically confirmed for our specific model, it is expected to be a system-dependent feature.
- [45] W. Yuan, Q. Zhu, T. Su, Y. Yao, W. Xing, Y. Chen, Y. Ma, X. Lin, J. Shi, R. Shindou, X. C. Xie, and W. Han, *Sci. Adv.* **4** (2018).
- [46] Z. Shen, Y. Xue, Z. Wu, and C. Song, *Phys. Chem. Chem. Phys.* **24**, 27612 (2022).
- [47] C. Xu, J. Feng, S. Prokhorenko, Y. Nahas, H. Xiang, and L. Bellaiche, *Phys. Rev. B* **101**, 060404(R) (2020).
- [48] K. Kim, S. Y. Lim, J.-U. Lee, S. Lee, T. Y. Kim, K. Park, G. S. Jeon, C.-H. Park, J.-G. Park, and H. Cheong, *Nat. Commun.* **10** (2019).
- [49] Z. Ni, A. V. Haglund, H. Wang, B. Xu, C. Bernhard, D. G. Mandrus, X. Qian, E. J. Mele, C. L. Kane, and L. Wu, *Nat. Nanotechnol.* **16**, 782 (2021).
- [50] A. Qaiumzadeh, H. Skarsvåg, C. Holmqvist, and A. Brataas, *Phys. Rev. Lett.* **118**, 137201 (2017).
- [51] T. Fukui, Y. Hatsugai, and H. Suzuki, *J. Phys. Soc. Jpn.* **74**, 1674 (2005).
- [52] S. A. Owerre, *J. Appl. Phys.* **121**, 223904 (2017).
- [53] P. A. Pantaleón and Y. Xian, *J. Phys.: Condens. Matter* **29**, 295701 (2017).
- [54] P. A. Pantaleón and Y. Xian, *J. Phys. Soc. Jpn.* **87**, 064005 (2018).